Hybrid Particle Brush Coatings with Tailored Design for Enhanced Dendrite Prevention and Cycle Life in Lithium Metal Batteries

Lara L. Dienemann¹, Rongguan Yin², Tong Liu², Adrien Stejer³, Verena Kempkes², Sipei Li⁴, Iryna V. Zenyuk³, Krzysztof Matyjaszewski², Matthew J. Panzer^{5*}

¹Department of Mechanical Engineering, Tufts University

Medford, MA 02155, USA

²Department of Chemistry, Carnegie Mellon University

Pittsburgh, PA 15213, USA

³Department of Chemical & Biomolecular Engineering, University of California Irvine; National Fuel Cell Research Center

Irvine, CA 92697, USA

⁴Ionic Materials, Inc.

Woburn, MA 01801, USA

⁵Department of Chemical & Biological Engineering, Tufts University

Medford, MA 02155, USA

Keywords: chemo-mechanics, lithium metal batteries, micro-computed tomography, artificial SEI, SI-ATRP, polymer hybrids, lithium dendrites

Abstract

Interfacing a lithium metal electrode with a designed thin-film coating offers promise in gaining control over plating and stripping instabilities during cycling, especially by inhibiting the growth of dendrites. This work introduces a coating comprised of hybrid particle brushes synthesized by grafting poly(poly[ethylene glycol] methyl ether methacrylate) from silica nanoparticles *via* surface-initiated atom transfer radical polymerization (SI-ATRP). Particle brushes in tetrahydrofuran solutions were drop cast on lithium metal and cycled in pouch cells with ether-based liquid electrolyte at 1 mA cm⁻² and 1 mAh cm⁻² which were then evaluated with synchrotron X-ray micro-computed tomography to understand corresponding lithium morphologies. The

coatings that achieved the longest cycle life (average of 275 cycles) avoided dendrites and densified the cycled lithium, both in early and late stages of cycling. *Postmortem* analysis of the failed cells compared the bare Li and coating-protected Li systems. Grafting densities (0.21 to 0.72 chains nm⁻²) of the particle brushes were optimized and enabled coatings exhibiting ionic conductivities similar to the liquid electrolyte system with slightly higher Arrhenius activation energies. Mechanical behaviors (modulus: 30 to 80 kPa; creep strain rate: approximately 10⁻⁴ s⁻¹) did not play a dominant role in improvement, suggesting that tuning the particle brush architecture mainly prevents dendrites through resulting ionic transport effects and more regulated plating/stripping behavior.

Introduction

As demand increases for better battery performance, it is crucial to move beyond the current generation of lithium-ion battery materials, *i.e.* transition-metal-oxide cathodes paired with graphite anodes. As these cells have almost reached their limit in terms of energy density and rate capability, fully replacing the graphite anode with lithium metal is a promising solution due to its high energy density, high theoretical capacity (3860 mAh g⁻¹, 2046 mAh cm⁻³), and low electrochemical potential. At the cell level, estimates from commercial cells show that lithium metal paired with high nickel content cathodes and liquid electrolytes can deliver roughly twice the gravimetric and volumetric energy densities as graphite/lithium iron phosphate cells and twice the gravimetric energy density of silicon-graphite paired with lithium nickel cobalt aluminum oxide. However, the instabilities that arise from uneven plating and stripping at the lithium metal interface prevent lithium metal cells from achieving competitive cycle life for several applications such as transportation (electric vehicles, electric vertical takeoff and landing, etc.). In one failure

mode, lithium plates in preferential "hot spots" and strips away from other areas, resulting in mossy morphologies known as dendrites that degrade cell performance with partially conductive pathways between electrodes (soft shorts). Researchers are exploring how to mitigate this early onset failure mode by controlling the nucleation and deposition mechanism as well as by mechanically blocking the protrusion and propagation of dendrites.^{2,3} This is sought to be achieved by the addition of engineered materials that physicochemically stabilize the lithium metal anode.

One option is to replace the liquid electrolyte with a solid-state electrolyte having superior mechanical toughness. However, this requires hundreds of megapascals of stack pressure in order to maintain contact at the electrolyte-anode interface, sacrificing pack-level energy density and welcoming another failure mode involving lithium filaments plating into and propagating through cracks in the electrolyte. 4-6 On the other hand, interfacing lithium metal with liquids or plasticized polymers is considered to inadequately block dendrites due to poor mechanics.⁷ Ionic transport through polymers relies on segmental chain motion and hopping across coordination sites.⁸ This is conditional on the polymer being free of crystallinity, as crystalline domains do not participate in these ionic transport mechanisms. Combining ceramic and polymeric materials into a composite electrolyte is thought to reap the benefits of both materials, as ceramics have the mechanical properties necessary to push back against lithium protrusions, while plasticized polymer viscoelasticity helps to maintain contact with interfacing components.⁹ It was found that in the dendrite boundary condition of particle-polymer composite separators, sufficient stiffness to push back against lithium metal dendrites as well as flowability around these protrusions correlated with the most stable cycling. 10 Another finding was that homogeneity of the dispersion of particles in the polymer is necessary to prevent severe mossy lithium. 10 Even in plain liquid or solid-state electrolyte systems, agglomeration of ions or defects in the ceramic are segues to cell failure by means of lithium plating and stripping "hot spots." Thus, homogeneity is a critical prerequisite that can also be assumed for hybrid coating designs.

While dispersing ceramic particles within a polymer can deter its crystallinity, particle agglomerations, inhomogeneity at the lithium metal interface, and ceramic-polymer incompatibility are challenges. 10,11 It was found that the portion of amorphous polymer is responsible for ionic transport in hybrid composite separators. 10,12,13 The separators with larger amorphous polymer fractions had good interfacial compatibility with the particles and maximal interfacial area across those domains owing to fewer agglomerations. 10 One composite nanostructure in particular has the potential to completely avoid polymer crystallinity, particle agglomerations, and interface heterogeneity.¹⁴ This is comprised of polymer chains covalently attached, or grafted, onto/from nanoparticles. These "particle brushes" have been studied previously in the battery literature with a variety of polymer chemistries. 15-24 In one approach, 5 kg mol⁻¹ polyethylene oxide (PEO) was functionalized with a silane group and condensed onto silica nanoparticles. 25,26 Plasticized with lithium bis(trifluoromethylsulfonyl)imide (LiTFSI) salt, it improved capacity retention of lithium metal cells cycled at 0.2 mA cm⁻². As for mechanics, it was found that interparticle interactions resulted in caging, where friction between particles has a yielding effect per applied stress.^{24,27} Interparticle interactions were found to be tunable by adjusting the architecture of the particle brushes. However, it was proposed that if the grafting density is high enough to discourage mechanical interactions, the ionic conductivity is improved and results in a superior electrolyte. ^{28,29} Another study used surface-initiated atom transfer radical polymerization (SI-ATRP) to attach polyacrylonitrile to yttria-stabilized zirconia nanoparticles, which demonstrated improved capacity retention as a lithium metal coating when the cell was cycled at a 1C rate over 50 cycles with an ether based liquid electrolyte.²² The advantages of SI-

ATRP include but are not limited to high precision control over grafting density of the particle brush, as well as the molecular weight and polydispersity of the polymer.^{30–36}

While the discussed studies show promising lithium metal results, extended cycle life has mainly been reported for low current densities, low cycling capacities, and elevated testing temperatures (see Table S1, Supporting Information). Additionally, the impact of the architecture of the particle brush systems on dendrite prevention and overall failure mechanism is often overlooked. This study aims to address the importance of structure-property relationships in a ceramic-polymer nanostructured, agglomeration-controlled lithium metal coating in a liquid electrolyte system. Here, a poly(poly[ethylene glycol] methyl ether methacrylate) (poly(PEGMA₅₀₀)) architecture is grafted onto silica nanoparticles. A previous report by Rosenbach et al. compared ionic conductivity values between poly(PEGMA) bottlebrushes and linear PEO systems.³⁷ Another study used PEGMA-grafted hypercrosslinked porous poly(4chloromethylstyrene) nanoparticles as a lithium metal coating to improve performance.³⁸ In our system, the PEGMA side chains are roughly nine ethylene oxide units in length, which is below the polymer's entanglement limit.³⁹ This means that the PEO portions of these brushes are long enough to coordinate lithium ions and do not have too much length where mobility is constrained. We investigate the influence of grafting density and molecular weight (resultingly, inorganic content) on pouch cell-relevant mechanical properties, ionic conductivity, cycle life, and cycled lithium morphology as characterized by X-ray micro-computed tomography (micro-CT). As a result of this study, a significant improvement in lithium metal cycle life owing to densified lithium plating and stripping is obtained via specific particle brush architectures. A mechanism for this performance improvement seen in the studied system and whether it relies more heavily on

chemical or mechanical effects is suggested. Lastly, the observed shift in the failure mechanism for lithium metal cells with particle brush coatings is discussed.

Experimental

Particle Brush Synthesis and Characterization

Surface-initiated atom transfer radical polymerization (SI-ATRP), specifically using the activators regenerated by electron transfer (ARGET) approach, covalently grafted chains of poly(poly[ethylene glycol] methyl ether methacrylate), poly(PEGMA₅₀₀), (structure in Fig. 1) from 15.8 nm diameter silica nanoparticles (Nissan Chemical).⁴⁰ This approach enables low concentrations of the copper catalyst as well as tolerates limited oxygen exposure.^{14,41,42} The particles were first modified with bromide (Br) end groups similarly as performed in prior work.^{43,44} The polymerization was performed with copper(II) bromide catalyst (Cu^{II}Br₂, 99.9%, Aldrich), ligand tris[2-(dimethylamino)ethyl]amine (Me₆TREN, 99%, Alfa), and reducing agent tin(II) 2-ethylhexanoate (Sn(Oct)₂, 95%, Aldrich) with the poly(ethylene glycol) methyl ether methacrylate monomer, PEGMA₅₀₀ ($M_n = 500$ g mol⁻¹, Aldrich) initiating from the surface-modified particles. The resulting particle brushes were purified and dispersed in tetrahydrofuran (THF, 99.5%, Aldrich) via dialysis. Molecular sieves (3 Å, Aldrich) were added to remove residual water in the particle brush solution in THF. Water content was confirmed to be negligible with Karl Fischer titration.

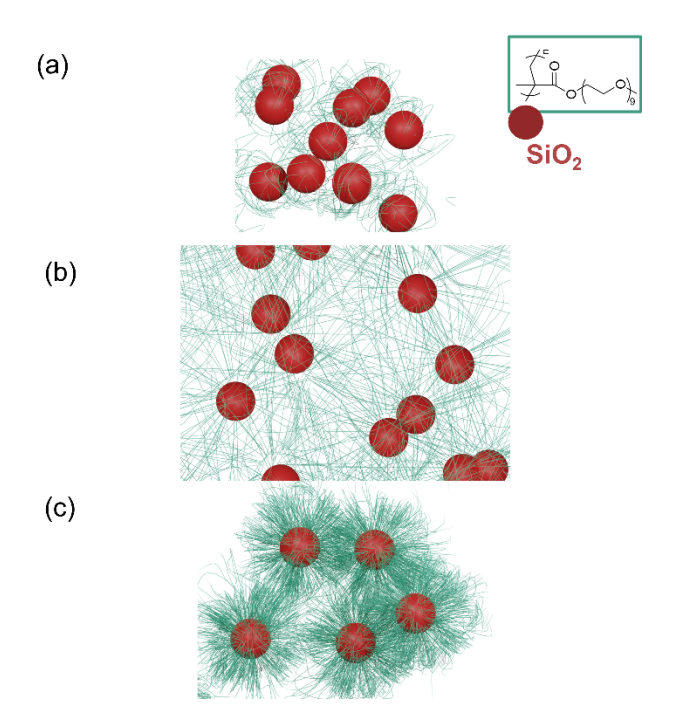


Figure 1. Schematic illustration of particle brush systems with varying grafting densities but similar molecular weights of tethered brush layers. Red spheres represent silica, and turquoise hairs represent the polymer domain. Grafting densities span (a) low, (b) intermediate, and (c) high values. Inset to panel (a) shows the grafted polymer repeat unit structure.

Molecular weight and inorganic content were directly measured with gel permeation chromatography (GPC) and thermogravimetric analysis (TGA) respectively. Prior to GPC, the synthesized particle brushes were left in a 48% hydrofluoric acid (HF, 99.99%, Aldrich) solution overnight to completely etch away the silica nanoparticles. GPC was run with Perfect Separations System (PSS) equipment with an Agilent 1260 Infinity II isocratic pump and a PSS SLD2020 multi-angle light scattering (MALS) refractive detector using PSS GRAM analytical columns on the remaining polymer with *N*,*N*-dimethylformamide (DMF, 99.9%, Acros) containing 0.05 M

LiBr as the eluent and linear PMMA standards for calibration. The reported molecular weights (M_n) are adjusted with the Mark-Houwink calibration to this particular eluent.⁴⁵

Post-polymerization, TGA samples were prepared by evaporating THF until the solution became a soft solid. A TA Instruments TGA 550 using air atmosphere was used to quantify the inorganic content fraction of the particle brushes, f_{inorg} , which then enabled the calculation of grafting density, GD, given Avogadro's number N_A , the silica density ρ (2.2 g cm⁻³) and diameter d (15.8 nm) of the bare nanoparticles (see Eq. 1). The procedure is the following: (1) ramp at 20 °C/min to 120 °C; (2) hold at 120 °C for 10 min; (3) high-resolution ramp at 20 °C/min to 800 °C; (4) hold at 800 °C for five minutes. The inorganic content was calculated after exclusion of residual solvent.

$$GD = \frac{(1 - f_{inorg})N_{A}\rho d}{6f_{inorg} M_{n}} \tag{1}$$

The electrolyte uptake by the polymer phase in the particle brushes was measured by weight then converted to volume given the density of silica nanoparticles and inorganic content of particle brushes. Mass measurements were taken of the solid particle brushes before and after a small volume of electrolyte (1M LiTFSI in 1,3-dioxolane (DOL) and dimethoxyethane (DME) at a ratio of 1:1 v/v + 1 wt% LiNO₃) was added to allow for swelling while excess liquid was removed.

Bulk mechanics were measured with a Dynamic Mechanical Analysis instrument (DMA) (DMA850, TA Instruments). A compression experiment was designed to mimic the mechanical conditions of vacuum sealing a pouch cell (ramping the stress to 0.03 MPa and holding at this stack pressure for 20 minutes.) The pressure of 0.03 MPa was selected, as 0.1 MPa (hydrostatic pressure in a pouch cell) required a force outside the limits of the DMA. Samples consisted of drop

cast particle brush coatings on 20 μ m lithium plated on copper foil (Honjo). Stiffness and creep rate were measured in the dry state and as swollen with electrolyte (1M LiTFSI in DOL:DME (1:1 v/v) + 1 wt% LiNO₃). The stiffness was estimated as 0.03 MPa divided by the final resulting compressive strain at the end of the stress ramp step. A bare lithium foil sample was also measured with this technique to differentiate the thickness of the coating.

Electrochemical Performance

The following was carried out in a dry room with moisture and temperature controlled at 20 ppm and 21 °C. The suspended particle brushes were mixed with LiTFSI at a weight ratio of LiTFSI:poly(PEGMA₅₀₀) of 50 percent. The solution was drop cast onto freestanding lithium foils (Albemarle, about 180 µm thick) which had been calender rolled between pouch cell material and cut into electrodes. The remaining THF in the drop cast coatings was left to evaporate with gentle heating on a hot plate for an hour. The cell design was adapted from our previous work which enabled high quality micro-computed tomograms of lithium metal batteries. ¹⁰ In this case, two 17 mm diameter Celgard 3501 separators (Celgard) were sandwiched by electrodes which achieved the minimum electrode separation requirement (50 µm) for optimal micro-CT resolution of lithium metal in its various morphologies. For symmetric lithium metal cells, a 14 mm diameter active area was used. Before pouch cell sealing, 70 μL of 1M LiTFSI in DOL:DME (1:1 v/v) + 1 wt% LiNO₃ electrolyte was injected. Cells were left to rest for 12 hours before cycling with LANDt CT2001A (Landt Instruments) or Neware CT-4008T 5V20mA (Neware) battery testing equipment at 1 mA cm⁻² and 1 mAh cm⁻² at 25 °C. Cells rested for 30 minutes after each charge and discharge. Excess stack pressure was not applied.

To perform temperature dependent ionic conductivity experiments, coin-in-pouch cells were constructed in the dry room. The same thicknesses of the coatings studied in the pouch cell

batteries were drop cast onto stainless steel electrodes which also sandwiched a Celgard 3501 separator. A 50 µL amount of the same ether based liquid electrolyte that was used for cycling was injected before sealing a pouch around the stackup. Electrochemical impedance spectroscopy (EIS) was used to measure resistance values at 0, 20, 40, 60, 80, and 90 °C with an environmental chamber that allowed for temperature equilibration using a thermocouple that also measured temperature throughout the experiment.

Micro-computed Tomography

X-ray CT was carried out at the Advanced Light Source (Lawrence Berkeley National Laboratory, Berkeley) beamline 8.3.2. Camera optics were set at 10x magnification, resulting in 0.7 μm/pixel image resolution. An energy of 25 keV was selected with 200 ms exposure times and 1300 back projections were collected per 180-degree scan. The reconstructions and phase retrieval were done using Gridrec Algorithm with open source Tomopy. 46 Image stacks were processed and visualized with ImageJ 1.53q and segmented with Dragonfly version 2022.1.0.1259 (ORS Inc.).

Results & Discussion

Particle Brush Characterization

Particle brushes are classified by the length of the polymer chains (molecular weight, M_n) and the density of polymer chains attached to the nanoparticle surface (grafting density, GD). The TGA and GPC traces from Mn40-GD0.46 (molecular weight = 40 kg mol⁻¹, grafting density = 0.46 nm⁻²) particle brushes are shown in the Supporting Information, Fig. S1. The molecular weight, grafting density, inorganic content, and polydispersity of all studied polymer brushes are summarized in Table S2.

On a microstructural level, the homogeneity of the as-drop cast coatings is found to be improved by the covalent attachment of the polymers onto the nanoparticles. In comparison, when bare silica nanoparticles are blended with free polymer chains, crystalline agglomerations characteristic of PEO are present in tapping mode AFM (see Fig. S2c). The coating with the same polymer concentration and molecular weight grafted from nanoparticles displays a homogeneous dispersion of particle brushes, seen in Fig. S2b. This ensures that the particle brush coating would not promote dendrites due to local variations of current density resulting from heterogeneity at this length scale.

Controlling the thickness of the particle brush layer is a challenge, as the coating swells differently depending on particle brush architecture and layer packing. As drop cast, an ion milled cross section of the particle brushes on lithium is around 300 nm thick (see Fig. S3). The same volume of drop cast particles along with LiTFSI added in 50 percent of poly(PEGMA₅₀₀) by weight expands the thickness by an order of magnitude. A similar effect occurs when introducing liquid electrolyte to the coating in the battery, which is further discussed below. Therefore, the swollen particle brush coating thickness could not be accurately controlled in this study and is measured for each coating in the swollen state (see Fig. S4).

Extended Cycling

Symmetric galvanostatic cycling performance was evaluated for cells with both lithium metal electrodes coated with several variations of particle brushes. The raw cycling data shown in Fig. 2a highlights the difference in cycling behavior between the cell with bare lithium electrodes and the cell with the particle brush coating *Mn40-GD0.46*. The overpotentials seen in the waveforms of the coated lithium cell are lower than that of the bare lithium cell. The bare lithium cell also demonstrates asymmetry in its overpotentials until 400 hours, when the negative

overpotentials experience a significant drop in absolute value followed by a gradual increase in absolute overpotential. This type of asymmetric and unstable behavior from bare lithium is characteristic of dendrite formation and uneven solid electrolyte interphase (SEI) growth. On the contrary, the cell behavior of Mn40-GD0.46 throughout the cycles plotted in Fig. 2a shows insignificant deviations in overpotential. The resulting failure of this cell is shown in Fig. S5f; it is not a result of soft shorting due to dendrites but rather depletion of the lithium reservoir.⁴⁷

Cell failure is analyzed for each coating tested with extended symmetric lithium metal cycling at 1 mA cm⁻² and 1 mAh cm⁻². Performance is evaluated by "cycles to failure," which is defined as the cycle at which one of the following occurs: (1) a polarization of 0.6 V ("hard short" if sudden, see red data in Fig. S5f; depletion of electrolyte and/or lithium reservoir if gradual), (2) a drop followed by a gradual increase in overpotential (see black, blue, and green data in Fig. S5f), or (3) a significant drop in overpotential followed by flat, square-like potential waveforms; the latter two represent "soft short". 47,48 It is important to note that although a few different types of failure modes are classified here, the failure mechanism of the symmetric lithium cells is often a combination of multiple above-mentioned scenarios. 48,49 Figure 2b contains these results in a 3D bar graph which compares the cycle life to particle brush architecture (M_n, GD) . Bare lithium performance is also indicated on this plot, located at the x-y origin. It can be noted that while some particle brushes significantly outperform bare lithium—especially Mn40-GD0.46—other coatings worsen lithium metal cycle life. The average cycle life observed for the bare lithium cells was 59 cycles, while the average of the coated cells was 275 cycles. The important particle brush architecture variable which exhibits a trend with lithium metal cycle life is grafting density; a 2D plot highlighting this relationship is in Fig. 2c. Plots comparing molecular weight and inorganic content show no obvious trends (see Fig. S6, Supporting Information).

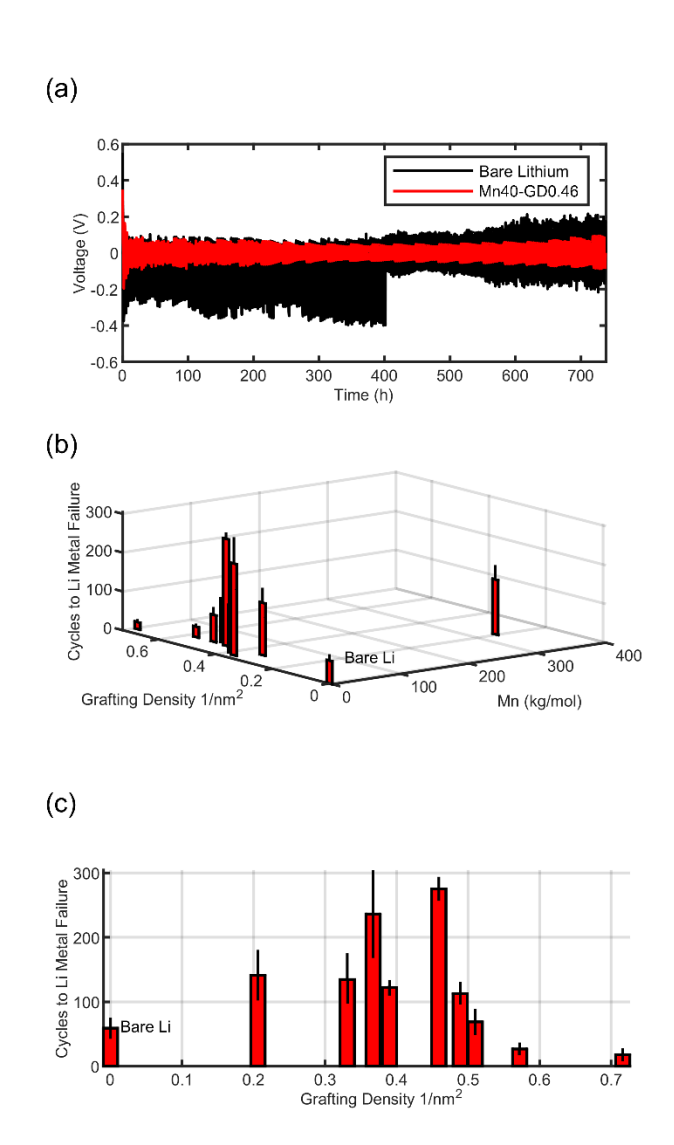


Figure 2. Symmetric lithium cycling at 1 mA/cm² and 1 mAh/cm² in CT-ready pouch cells. (a) Voltage vs. time data comparing uncoated (bare) lithium cells to cells with Mn40-GD0.46 coating on both lithium electrodes. The plot shows 246 cycles. (b) Cycle life is compared for varying M_n and GD within different coatings. Cycle at cell failure is defined as the cycle at which a polarization of \pm 0.6 V or abrupt decrease in absolute potential characteristic of a soft short. The bare lithium system is plotted at M_n and GD values of zero. (c) Cycles to failure plotted versus grafting density. Error bars denote sample standard deviations in panels (b) and (c).

Ex-situ synchrotron X-ray tomography can be used to verify the mechanism by which lithium metal cycle life is extended using the best particle brush coatings. Imaging lithium metal cells with X-ray computed tomography poses challenges, as lithium's low atomic number results in low X-ray attenuation, especially when imaged alongside denser materials.^{50–53} As seen in the cell cross sectional image slices in Fig. 3a-d, the cell configuration used in this study produces scans with clear and reproducible representations of lithium metal structures including porosity (dark voxels) and pits (brighter voxels making up hemispheres). Qualitatively, lithium metal with mossy morphology is captured most prominently in Fig. 3a-b, where the bare lithium symmetric cell has endured one charge-discharge cycle (Fig. 3a) and after 20 cycles (Fig. 3b). Notably, after a single cycle, mossy lithium that has been plated during the first charge does not strip away during the first discharge, beginning the accumulation of mossy lithium whose progression is evident after 20 cycles. Contrastingly, with particular particle brush coatings (Mn40-GD0.33 and Mn40-GD0.46) which improved cycle life in these cells, less mossy lithium is observed following the initial cycles (see Fig. 3c-d). This effect is also present in later cycles (see Fig. S5a,c). Throughout the X-ray CT scan of the cell with Mn40-GD0.33 having cycled once, lithium morphology was not distinguishable from the bulk lithium electrodes, meaning that lithium has plated densely, without pores. The lithium/coating interface is also smooth without evidence of pitting during stripping on either electrode. Comparing Fig. 3a with Fig. 3c demonstrates how severe a disadvantage the uncoated lithium metal is already at after just a single charge and discharge of the cell.

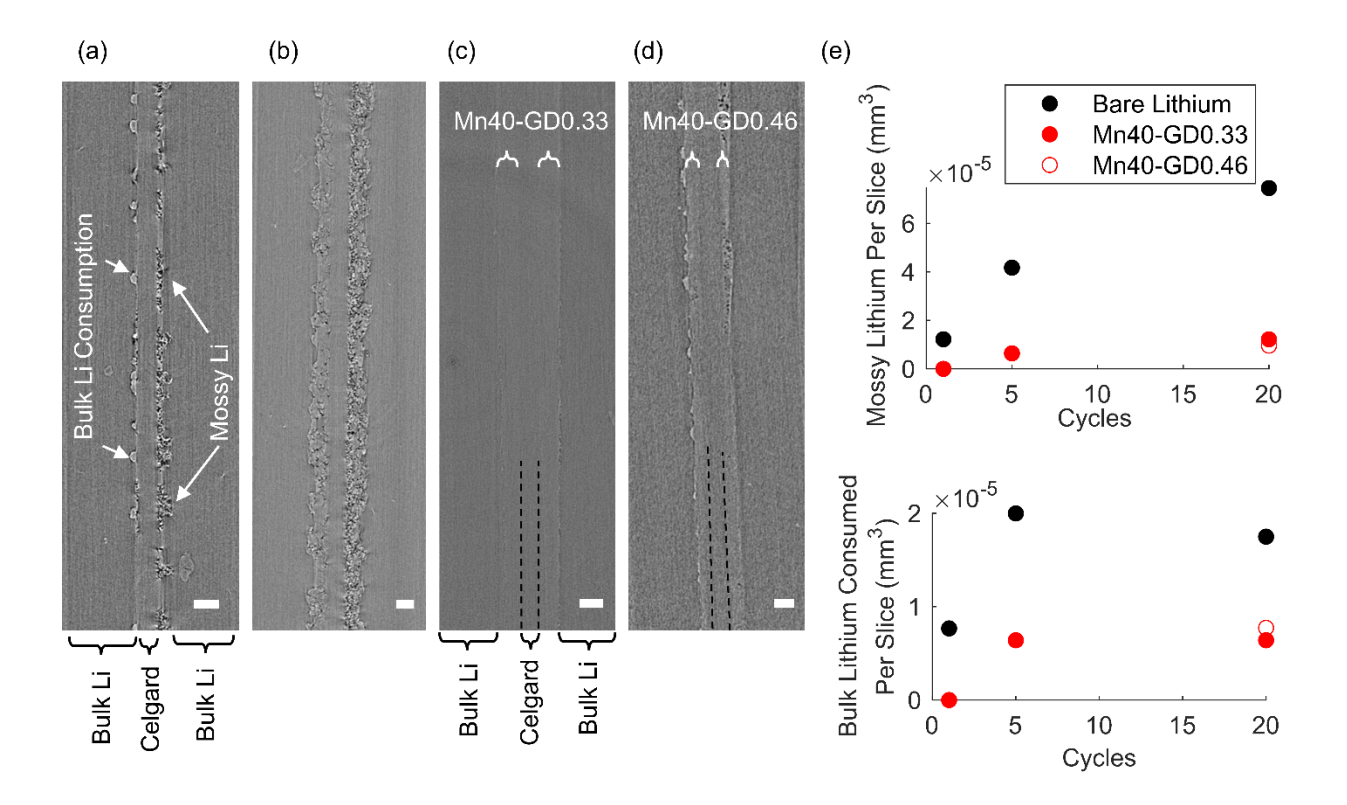


Figure 3. (a-d) *Ex-situ* X-ray tomography cross sectional slices of lithium symmetric cells cycled at 1 mA/cm² and 1 mAh/cm². (a) Bare lithium cell post 1 cycle. Examples of mossy (dendritic) lithium and areas where bulk lithium has been consumed (stripped and not replaced) labeled with arrows. Bulk of lithium electrodes and Celgard separators labeled with brackets. (b) Bare lithium cell post 20 cycles. (c) Cell with *Mn40-GD0.33* coating on both electrodes post 1 cycle. Coating labeled with white brackets. Black dotted lines distinguish separator/coating interfaces. (d) Cell with *Mn40-GD0.46* coating on both electrodes post 20 cycles. Coating labeled with white brackets. Black dotted lines distinguish separator/coating interfaces. (e) Image segmentation data plotted over cycles 1, 5, and 20 comparing bare lithium cell to cells with *Mn40-GD0.33* and *Mn40-GD0.46* coatings. Volume of mossy lithium divided by total slices segmented in CT scan (top), volume of bulk lithium consumed divided by total slices segmented in CT scan (bottom). Scale bars: 100 μm.

The cell with the coating which achieved the longest cycle life in symmetric lithium cells (Mn40-GD0.46) was imaged after 20 cycles, and a representative view of the corresponding cycled lithium morphology is shown in Fig. 3d. Some islands of mossy morphology have been left behind, and pitting is also noticeable at this stage. While these features are visually less prominent than in the bare lithium image, the X-ray CT scans are evaluated with segmentation to quantify the extent of the mossy lithium and pitting. The scans shown in Fig. 3a-d, as well as cells cycled five times and the Mn40-GD0.33 cell after 20 cycles were segmented for volume of mossy lithium (voxels containing void space as well as brighter voxels surrounding these voids, denoted as "Mossy Li" in Fig. 3a), as well as volume of bulk lithium consumed. In the scans with the least amount of mossy lithium, segmentation of bulk lithium consumed was performed by establishing the original boundary of the active lithium metal electrode area which maintained its visibility due to the island-like nature of lithium deposition and stripping at this stage. In the scans where the original lithium metal electrode boundary is entirely consumed, it was estimated under the assumption that its starting thickness was the same as observed in other cells and what was measured using a drop gauge (180 µm). Figure 3e displays plots summarizing the segmentation data that confirm what is seen in the single slices shown in Fig. 3a-d; lithium metal cells that are coated with either Mn40-GD0.33 or Mn40-GD0.46 contain less mossy lithium, and less of the bulk lithium electrodes are consumed. The X-ray CT slices illustrating the cross-sections of the bare lithium cell as well as the Mn40-GD0.33 cell after five cycles can be found in Fig. S7.

Furthermore, the bare lithium cell and the *Mn40-GD0.46* cell were scanned *postmortem*. In panels (a) and (c) of Fig. S5, it can be seen that even at the failure point (which occurred due to soft shorting at a much earlier stage), the uncoated lithium system accrued a much more expansive volume of mossy lithium. However, in both uncoated and coated systems, the lithium reservoir is

depleted at failure. The corresponding cycling data in Fig. S5f supports that the coating that promotes the longest cycle life in the studied sample set shifts the failure mode of the lithium metal away from the combination of ongoing soft shorting due to abundant mossy structures and liquid electrolyte depletion. As the volume of mossy lithium is always less in the coated cell and the bulk lithium is being consumed at a slower rate, upon depletion of the lithium reservoir, less liquid electrolyte has been consumed by mossy lithium, which results in the sudden polarization at the end of cell life rather than the gradual increase of the polarization seen in the bare lithium data.⁴⁷ This slowing-down failure effect is studied for the *Mn40-GD0.33* coating in symmetric lithium cells with a carbonate-based liquid electrolyte (Fig. S8) as well as in lithium vs. lithium titanate (LTO) half cells (Fig. S9) with slight differences in each separate system. Notably, the failure mode of the half cells (cycled at C/4, 3.1 mAh cm⁻²) without the coating always involved a significant dendrite resulting in increasing charge capacity and therefore a sudden drop in Coulombic efficiency.⁵⁴ The coated lithium electrode cells never displayed such protrusions in the X-ray CT scans or in cycling data.

The particle brush coating was further challenged by being paired with a carbonate-based liquid electrolyte in lithium symmetric cells, which were cycled using the same conditions as the symmetric cells with ether-based electrolyte. Carbonates are known to passivate the lithium surface less preferentially compared to ethers, stressing the system sooner during cycling.⁵⁵ The X-ray CT scans of the cells with carbonate electrolyte (example in Fig. S8b) show less conversion of bulk lithium into mossy lithium in coated systems compared to the uncoated cells.

Further supporting the mechanism of cycle life improvement via cycled lithium densification in coated lithium cells, digital images of cell tear downs (Fig. S10) show the differences in coated versus uncoated systems across cycles. Looking top-down on the lithium

electrodes as well as the separators removed from the cells, the shade of the cycled lithium is lighter gray and shinier for the coated electrodes, while the bare lithium electrodes all are black and heterogeneous. Furthermore, the imaged separators removed from the bare lithium cells are covered with embedded dendrites which have broken off easily from the weak and brittle mossy structure of the cycled lithium. On the other hand, this happens to the separators present in the coated lithium cells to a much lesser extent.

Physicochemical Properties

As different designs of the studied particle brush coatings were observed to either improve or worsen the lithium metal cycle life while also varying the corresponding cycled lithium morphology (Fig. S5), understanding the mechanism by which this occurs is crucial for optimizing lithium metal coating design. To this end, correlations are sought across particle brush design values and measured coating properties that support the hypothesis that dendrites can be either mitigated through the prevention of their formation or by mechanically blocking their propagation. Four of the synthesized particle brush systems were characterized in detail; three of these had similar polymer molecular weights while spanning three different grafting densities and extended cycling performances (Mn40-GD0.33, Mn40-GD0.46, and Mn43-GD0.57), and one had a much larger polymer molecular weight than the others (Mn329-GD0.21).

These four different particle brush architectures span four different inorganic content values, which are summarized in Fig. 4a. The amount of liquid electrolyte uptake by the polymer phase of the particle brush coatings is also indicated in this plot. The data show the expected relationship that the more polymer present in the coating (*i.e.* lower inorganic content), the more swollen the polymer phase will become when introduced to the ether-based electrolyte.

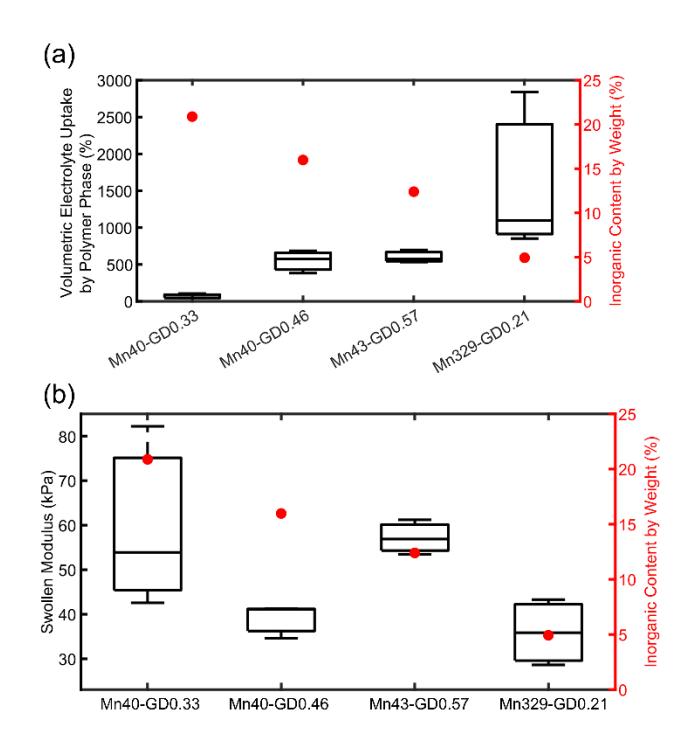


Figure 4. Physical properties of *Mn40-GD0.33*, *Mn40-GD0.46*, *Mn43-GD0.57*, and *Mn329-GD0.21* coatings. (a) Electrolyte uptake of polymer phase by volume (left axis); inorganic content by weight (right axis). (b) Swollen modulus measured with DMA (left axis); inorganic content by weight (right axis).

It is expected that, in general, swollen particle-polymer composites with higher inorganic content and less electrolyte uptake exhibit larger stiffness. The results from the DMA tests on particle brushes, however, do not show a correlation. The particle brush systems swollen with liquid electrolyte underwent compression at rates similar to those experienced by the battery stack up during pouch cell construction; the resulting estimated stiffnesses are plotted in Fig. 4b. Inorganic content is also plotted on the right axis, unveiling a lack of relationship with mechanics. The particle brushes which improved the baseline lithium metal performance all demonstrate much

lower stiffness (30-80 kPa) than lithium metal itself and other researched coatings whose modulus is cited as a dendrite suppressing trait (~GPa).⁵⁶⁻⁵⁸ Even when the particle brushes are in the dry state (no liquid electrolyte present), the modulus measured with DMA does not exceed 200 kPa (Fig. S11b), and the Sneddon modulus determined from PeakForce Quantitative Nanomechanical Analysis (QNM) AFM measurements does not exceed the MPa range (Fig. S12). Creep was also investigated with DMA, as it has been discussed in the literature that the viscoelasticity of polymer electrolytes can help physically maintain their interface with lithium metal, preventing heterogeneous void formation which can be "hot spots" of ion flux.⁵⁹ While the polymers in the particle brush system create observable viscoelastic behavior, differences in creep rate (on the scale of 10⁻⁴ s⁻¹)—the most relevant measurement due to the relatively constant pressure boundary conditions of a pouch cell—were not observed (see Fig. S11c).

While mechanics were found to not correlate to lithium metal cycling performance, properties related to ionic transport shed light on relevant improvement mechanisms. Figure 5a indicates that the coatings which improved baseline lithium cycling (*Mn40-GD0.46* and *Mn329-GD0.21*) maintain ionic conductivity in the mS cm⁻¹ range throughout the measured temperature range (0-90 °C; see also Fig. S13 with 80 and 90 °C measurements with deviations from Arrhenius behavior). The ionic conductivity values of these two coatings are fairly similar to those of the liquid electrolyte across the temperature range studied. Interestingly, *Mn40-GD0.46* has significantly longer cycle life yet lower ionic conductivity than *Mn329-GD0.21*. Likewise, the range of estimated activation energies calculated from the Arrhenius relation are lowest for *Mn329-GD0.21* and most comparable to the activation energies estimated for the liquid electrolyte (Fig. 5b). This can be attributed to the highest content of liquid electrolyte taken up by the polymer in *Mn329-GD0.21*.

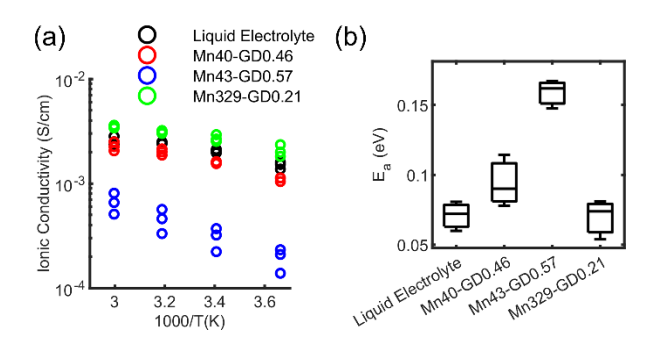


Figure 5. Temperature dependent ionic conductivity data comparing *Mn40-GD0.46*, *Mn43-GD0.57*, and *Mn329-GD0.21* swollen particle brush coatings. (a) Ionic conductivity plotted as a function of inverse temperature. (b) Activation energy values, which were obtained via Arrhenius model best-fits to the ionic conductivity data.

It has been previously proposed that a polymer additive within a liquid electrolyte, while slightly reducing the ionic conductivity, can control the progression of local inhomogeneities by dampening ion transport near the electrode interface. This may explain why a coating that slightly reduces ionic conductivity compared to the liquid system can lead to an improved cycle life. Therefore, it is reasonable to conclude that the mobile PEO units of the polymer chains that participate in ionic transport are effectively slowing it down. The mobility of the polymer and its ability to dissociate and transfer lithium ions across its coordination sites is a result of a balance between the free volume and the distance between chains. This is closely related to the grafting density of the particle brushes. On one end of the spectrum, a high grafting density, while shortening the distance between chains, reduces free volume in the system as well as increases tortuosity of the pathway of lithium ion coordination structures must take. This may slow down the overall lithium ion transport too much at the tested rates, which could explain the worsened performance by *Mn43-GD0.57*. On the other hand, grafting density that is too low poses different

challenges such as an excessive space between chains and not enough overall polymer concentration to effectively dissociate ion clusters in a liquid-rich system. It is worth mentioning that lower grafting density results in a greater exposed surface area of silica nanoparticles. The silica surface has Lewis acidic character which can also help with ion dissociation while being itself unable to contact and react with the lithium metal surface, in the case of the particle brushes.⁶¹ These effects at the two extreme ends of grafting density may explain the optimization curve seen in the relationship in Fig. 2c, where improved cycle life skews towards lower grafting densities with the most significant improvement shown by an intermediate grafting density. This relationship may be particular to the poly(PEGMA₅₀₀) polymer design, as prior literature on particle brushes with linear PEO are optimized by maximizing grafting density or by introducing additional unconstrained polymers, with good performance resulting from a higher degree of separation and fewer interactions between particles.^{22,28,29,62}

The proposed mechanism for lithium metal cycle life extension by densification of cycled lithium morphology via the particle brushes in this study appears to favor dendrite prevention rather than by suppressing dendrite growth due to mechanical stiffness. This preventative mechanism consists of participation in ionic transport from the polymer regime of the particle brushes, which is optimized for a particular grafting density. When introduced to the ether-based liquid electrolyte used in this study, the PEGMA₅₀₀-based polymer brushes grafted from silica nanoparticles can harmoniously dissociate lithium ions and pass them across coordination structures. The homogeneous arrangement of particle brushes and lack of agglomeration of particles promotes this effect to occur evenly through the swollen particle brush layer.

It remains in question whether further improvement may be possible by designing the system to also be effective at mechanically blocking dendrite growth. It was found that for particle-

polymer separators, both ion transport homogeneity and mechanical enhancements should be key design considerations to achieve better lithium metal cycling.¹⁰ An additional coating was synthesized that consisted of an in-situ crosslinked matrix of poly(ethylene glycol) diacrylate (PEGDA, $M_n = 575$ g mol⁻¹) scaffolding the swollen particle brushes. While it was initially hypothesized that this crosslinked PEGDA scaffolding would provide higher mechanical stiffness and resistance to creep, the measured mechanical properties were not found to be very different compared to the particle brush system (see Fig. S14). Intriguingly, the containment of the particles by this scaffolding, while still improving the cycle life by decreasing mossy lithium from the bare lithium baseline, resulted in heterogeneous stripping behavior (Fig. S14d). In these PEGMA₅₀₀based particle brush systems which rely on some amount of ionic transport in the polymer, mechanical enhancements likely diminish the mobility required of the polymer to facilitate the establishing and breaking of Li⁺ ion coordination structures. Future work on these as well as novel particle brush designs will explore a wider range of molecular weights, grafting densities, and polymer architectures which can transport lithium effectively in different electrolytes, hoping to reveal more about their mechanistic impact on lithium metal battery performance and failure modes. Further improvements to lithium metal coating design are expected to further extend cell cycle life and further delay the non-dendritic failure modes.

Conclusion

In this study, novel particle brushes were synthesized and evaluated as coatings for lithium metal battery electrodes. The objective was to investigate the impact of different particle brush architectures on the cycle life of symmetric cells, particularly during early stage cycling with etherbased liquid electrolyte. The findings revealed that specific particle brush structures effectively controlled the density of cycled lithium morphology as evaluated with micro-CT, leading to as

much as a four-fold increase in cycle life. The failure mode observed in the coated Li cells was not attributed to dendrite formation, but rather to the consumption of lithium due to the intensive cycling and prolonged cycle life, which further indicates the effectiveness of the coating. The best performance was obtained by optimizing the grafting density of the particle brushes, which promoted effective ionic transport through the coating by facilitating adequate polymer participation. Surprisingly, the mechanical behaviors of the coatings were not critical to dendrite mitigation, indicating a stronger reliance on dendrite prevention than on dendrite blocking to improve cycle life. Overall, this research sheds new light on the design of particle brush coatings and their marked improvement of the performance of lithium metal batteries with liquid electrolytes.

Supporting Information

The Supporting Information is available free of charge at XXX.

• Comparative literature data table, particle brush synthesis, thermogravimetric analysis, gel permeation chromatography, atomic force microscopy, scanning electron microscopy, extended cycling with end of life, *postmortem* X-ray micro-computed tomography, inorganic content and molecular weight vs. cycle life, X-ray CT after 5 cycles (bare lithium and *Mn40-GD0.33*), carbonate electrolyte data, lithium titanate (LTO) half cell data, cell tear downs, mechanical properties, ionic conductivity, and scaffolded coating data.

Notes

The authors declare no competing financial interest.

Acknowledgments

The authors would like to thank Ionic Materials, Inc. for financial support as well as the use of their facilities and testing equipment throughout this work. This research used the resources of the Advanced Light Source (ALS). The ALS is supported by the Director, Office of Science, Office of Basic Energy Sciences, of the U.S. Department of Energy under Contract No. DE-AC02-05CH11231. We thank Dr. Dula Parkinson and Hasitha S. Wijesuriya for their assistance at the 8.3.2 beamline at ALS. R.Y. and K.M. acknowledge DE-SC0018784 for particle brush synthesis and characterizations. M.J.P. acknowledges support from the NSF under award DMR-2209500.

Corresponding Author

Matthew J. Panzer, Email: Matthew.Panzer@tufts.edu

References

- (1) Frith, J. T.; Lacey, M. J.; Ulissi, U. A Non-Academic Perspective on the Future of Lithium-Based Batteries. *Nat. Commun.* **2023**, *14* (1), 420. https://doi.org/10.1038/s41467-023-35933-2.
- (2) Fu, C.; Venturi, V.; Kim, J.; Ahmad, Z.; Ells, A. W.; Viswanathan, V.; Helms, B. A. Universal Chemomechanical Design Rules for Solid-Ion Conductors to Prevent Dendrite Formation in Lithium Metal Batteries. *Nat. Mater.* 2020, 19 (7), 758–766. https://doi.org/10.1038/s41563-020-0655-2.
- (3) Liu, T.; Wu, X.; Zhu, S.; Lorandi, F.; Ni, L.; Li, S.; Sun, M.; Bloom, B. P.; Waldeck, D. H.; Viswanathan, V.; Whitacre, J. F.; Matyjaszewski, K. Polymer-Stabilized Liquid Metal Nanoparticles as a Scalable Current Collector Engineering Approach Enabling Lithium Metal

- Anodes. *ACS Appl. Energy Mater.* **2022**, *5* (3), 3615–3625. https://doi.org/10.1021/acsaem.1c04106.
- (4) Ning, Z.; Jolly, D. S.; Li, G.; De Meyere, R.; Pu, S. D.; Chen, Y.; Kasemchainan, J.; Ihli, J.; Gong, C.; Liu, B.; Melvin, D. L. R.; Bonnin, A.; Magdysyuk, O.; Adamson, P.; Hartley, G. O.; Monroe, C. W.; Marrow, T. J.; Bruce, P. G. Visualizing Plating-Induced Cracking in Lithium-Anode Solid-Electrolyte Cells. *Nat. Mater.* 2021, 20 (8), 1121–1129. https://doi.org/10.1038/s41563-021-00967-8.
- (5) Monismith, S.; Qu, J.; Dingreville, R. Grain-Boundary Fracture Mechanisms in Li7La3Zr2O12 (LLZO) Solid Electrolytes: When Phase Transformation Acts as a Temperature-Dependent Toughening Mechanism. J. Mech. Phys. Solids 2022, 160, 104791. https://doi.org/10.1016/j.jmps.2022.104791.
- (6) Monismith, S.; Qu, J.; Dingreville, R. Electrochemically Induced Fracture in LLZO: How the Interplay between Flaw Density and Electrostatic Potential Affects Operability. *J. Power Sources* **2023**, *559*, 232646. https://doi.org/10.1016/j.jpowsour.2023.232646.
- (7) Monroe, C.; Newman, J. The Impact of Elastic Deformation on Deposition Kinetics at Lithium/Polymer Interfaces. *J. Electrochem. Soc.* **2005**, *152* (2), A396–A404. https://doi.org/10.1149/1.1850854.
- (8) White, R. P.; Lipson, J. E. G. Polymer Free Volume and Its Connection to the Glass Transition. *Macromolecules* **2016**, *49* (11), 3987–4007. https://doi.org/10.1021/acs.macromol.6b00215.
- (9) Li, S.; Lorandi, F.; Wang, H.; Liu, T.; Whitacre, J. F.; Matyjaszewski, K. Functional Polymers for Lithium Metal Batteries. *Prog. Polym. Sci.* 2021, 122, 101453. https://doi.org/10.1016/j.progpolymsci.2021.101453.

- (10) Dienemann, L. L.; Geller, L. C.; Huang, Y.; Zenyuk, I. V.; Panzer, M. J. Understanding Lithium Dendrite Suppression by Hybrid Composite Separators: Indentation Measurements Informed by Operando X-Ray Computed Tomography. ACS Appl. Mater. Interfaces 2023, 15 (6), 8492–8501. https://doi.org/10.1021/acsami.2c20787.
- (11) Barai, P.; Fuchs, T.; Trevisanello, E.; Kim, H. K.; Richter, F. H.; Janek, J.; Srinivasan, V. Reaction Current Heterogeneity at the Interface between a Lithium Electrode and Polymer/Ceramic Composite Electrolytes. ACS Appl. Energy Mater. 2023. https://doi.org/10.1021/acsaem.2c03059.
- (12) Li, Z.; Huang, H.-M.; Zhu, J.-K.; Wu, J.-F.; Yang, H.; Wei, L.; Guo, X. Ionic Conduction in Composite Polymer Electrolytes: Case of PEO:Ga-LLZO Composites. *ACS Appl. Mater. Interfaces* **2019**, *11* (1), 784–791. https://doi.org/10.1021/acsami.8b17279.
- (13) Horowitz, Y.; Lifshitz, M.; Greenbaum, A.; Feldman, Y.; Greenbaum, S.; Sokolov, A. P.; Golodnitsky, D. Review—Polymer/Ceramic Interface Barriers: The Fundamental Challenge for Advancing Composite Solid Electrolytes for Li-Ion Batteries. *J. Electrochem. Soc.* 2020, 167 (16), 160514. https://doi.org/10.1149/1945-7111/abcd12.
- (14) Yan, J.; Bockstaller, M. R.; Matyjaszewski, K. Brush-Modified Materials: Control of Molecular Architecture, Assembly Behavior, Properties and Applications. *Prog. Polym. Sci.* 2020, 100, 101180. https://doi.org/10.1016/j.progpolymsci.2019.101180.
- (15) Liu, X.; Mao, W.; Gong, J.; Liu, H.; Shao, Y.; Sun, L.; Wang, H.; Wang, C. Enhanced Electrochemical Performance of PEO-Based Composite Polymer Electrolyte with Single-Ion Conducting Polymer Grafted SiO2 Nanoparticles. *Polymers* 2023, 15 (2), 394. https://doi.org/10.3390/polym15020394.

- (16) Ranque, P.; Zagórski, J.; Accardo, G.; Orue Mendizabal, A.; López del Amo, J. M.; Boaretto, N.; Martinez-Ibañez, M.; Arrou-Vignod, H.; Aguesse, F.; Armand, M.; Devaraj, S. Enhancing the Performance of Ceramic-Rich Polymer Composite Electrolytes Using Polymer Grafted LLZO. *Inorganics* 2022, 10 (6), 81. https://doi.org/10.3390/inorganics10060081.
- (17) Zhan, H.; Wu, M.; Wang, R.; Wu, S.; Li, H.; Tian, T.; Tang, H. Excellent Performances of Composite Polymer Electrolytes with Porous Vinyl-Functionalized SiO2 Nanoparticles for Lithium Metal Batteries. *Polymers* **2021**, *13* (15), 2468. https://doi.org/10.3390/polym13152468.
- (18) Erabhoina, H.; Rosenbach, D.; Mohanraj, J.; Thelakkat, M. Solid Polymer Nanocomposite Electrolytes with Improved Interface Properties towards Lithium Metal Battery Application at Room Temperature. *Electrochimica Acta* **2021**, *387*, 138455. https://doi.org/10.1016/j.electacta.2021.138455.
- (19) Guo, Q.; Xu, F.; Shen, L.; Wang, Z.; Wang, J.; He, H.; Yao, X. Poly(Ethylene Glycol) Brush on Li6.4La3Zr1.4Ta0.6O12 towards Intimate Interfacial Compatibility in Composite Polymer Electrolyte for Flexible All-Solid-State Lithium Metal Batteries. *J. Power Sources* **2021**, *498*, 229934. https://doi.org/10.1016/j.jpowsour.2021.229934.
- (20) Lago, N.; Garcia-Calvo, O.; Lopez del Amo, J. M.; Rojo, T.; Armand, M. All-Solid-State Lithium-Ion Batteries with Grafted Ceramic Nanoparticles Dispersed in Solid Polymer Electrolytes. *ChemSusChem* 2015, 8 (18), 3039–3043. https://doi.org/10.1002/cssc.201500783.

- (21) Zhao, H.; Jia, Z.; Yuan, W.; Hu, H.; Fu, Y.; Baker, G. L.; Liu, G. Fumed Silica-Based Single-Ion Nanocomposite Electrolyte for Lithium Batteries. *ACS Appl. Mater. Interfaces* **2015**, *7* (34), 19335–19341. https://doi.org/10.1021/acsami.5b05419.
- (22) Li, S.; Liu, T.; Yan, J.; Flum, J.; Wang, H.; Lorandi, F.; Wang, Z.; Fu, L.; Hu, L.; Zhao, Y.; Yuan, R.; Sun, M.; Whitacre, J. F.; Matyjaszewski, K. Grafting Polymer from Oxygen-Vacancy-Rich Nanoparticles to Enable Protective Layers for Stable Lithium Metal Anode. *Nano Energy* 2020, 76, 105046. https://doi.org/10.1016/j.nanoen.2020.105046.
- (23) Wang, M.; Tian, L.; Cao, Y.; Su, Z.; Zhang, W.; Yi, S.; Zhang, Y.; Niu, B.; Long, D. Surface Positive-Charged Modification of Inorganic Fillers to Optimize Lithium Ion Conductive Pathways in Composite Polymer Electrolytes for Lithium-Metal Batteries. *J. Colloid Interface Sci.* 2022. https://doi.org/10.1016/j.jcis.2022.10.137.
- (24) Agrawal, A. Rheology, Structure and Transport Properties of Hybrid Hairy Nanoparticles and Their Applications. Ph.D., Cornell University, United States -- New York. https://www.proquest.com/docview/1827600131/abstract/C055900DEA8640D6PQ/1 (accessed 2023-03-30).
- (25) Choudhury, S.; Vu, D.; Warren, A.; Tikekar, M. D.; Tu, Z.; Archer, L. A. Confining Electrodeposition of Metals in Structured Electrolytes. *Proc. Natl. Acad. Sci.* **2018**, *115* (26), 6620–6625. https://doi.org/10.1073/pnas.1803385115.
- (26) Choudhury, S.; Stalin, S.; Deng, Y.; Archer, L. A. Soft Colloidal Glasses as Solid-State Electrolytes. *Chem. Mater.* **2018**, *30* (17), 5996–6004. https://doi.org/10.1021/acs.chemmater.8b02227.

- (27) Liu, X.; Utomo, N. W.; Zhao, Q.; Zheng, J.; Zhang, D.; Archer, L. A. Effects of Geometric Confinement on Caging and Dynamics of Polymer-Tethered Nanoparticle Suspensions.

 *Macromolecules** 2021, 54 (1), 426–439. https://doi.org/10.1021/acs.macromol.0c01448.
- (28) Utomo, N. W.; Deng, Y.; Zhao, Q.; Liu, X.; Archer, L. A. Structure and Evolution of Quasi-Solid-State Hybrid Electrolytes Formed Inside Electrochemical Cells. *Adv. Mater.* **2022**, *34* (32), 2110333. https://doi.org/10.1002/adma.202110333.
- (29) Choudhury, S.; Agrawal, A.; Wei, S.; Jeng, E.; Archer, L. A. Hybrid Hairy Nanoparticle Electrolytes Stabilizing Lithium Metal Batteries. *Chem. Mater.* **2016**, *28* (7), 2147–2157. https://doi.org/10.1021/acs.chemmater.6b00029.
- (30) Matyjaszewski, K.; Jakubowski, W.; Min, K.; Tang, W.; Huang, J.; Braunecker, W. A.; Tsarevsky, N. V. Diminishing Catalyst Concentration in Atom Transfer Radical Polymerization with Reducing Agents. *Proc. Natl. Acad. Sci.* 2006, 103 (42), 15309–15314. https://doi.org/10.1073/pnas.0602675103.
- (31) Wang, J.-S.; Matyjaszewski, K. Controlled/"living" Radical Polymerization. Atom Transfer Radical Polymerization in the Presence of Transition-Metal Complexes. *J. Am. Chem. Soc.* 1995, 117 (20), 5614–5615. https://doi.org/10.1021/ja00125a035.
- (32) Matyjaszewski, K.; Xia, J. Atom Transfer Radical Polymerization. *Chem. Rev.* **2001**, *101* (9), 2921–2990. https://doi.org/10.1021/cr940534g.
- (33) Patten, T. E.; Xia, J.; Abernathy, T.; Matyjaszewski, K. Polymers with Very Low Polydispersities from Atom Transfer Radical Polymerization. *Science* **1996**, *272* (5263), 866–868. https://doi.org/10.1126/science.272.5263.866.
- (34) Matyjaszewski, K. Advanced Materials by Atom Transfer Radical Polymerization. *Adv. Mater.* **2018**, *30* (23), 1706441. https://doi.org/10.1002/adma.201706441.

- (35) Matyjaszewski, K.; Tsarevsky, N. V. Nanostructured Functional Materials Prepared by Atom Transfer Radical Polymerization. *Nat. Chem.* **2009**, *1* (4), 276–288. https://doi.org/10.1038/nchem.257.
- (36) Matyjaszewski, K.; Tsarevsky, N. V. Macromolecular Engineering by Atom Transfer Radical Polymerization. *J. Am. Chem. Soc.* **2014**, *136* (18), 6513–6533. https://doi.org/10.1021/ja408069v.
- (37) Rosenbach, D.; Mödl, N.; Hahn, M.; Petry, J.; Danzer, M. A.; Thelakkat, M. Synthesis and Comparative Studies of Solvent-Free Brush Polymer Electrolytes for Lithium Batteries. *ACS Appl. Energy Mater.* **2019**, *2* (5), 3373–3388. https://doi.org/10.1021/acsaem.9b00211.
- (38) Li, S.; Huang, J.; Cui, Y.; Liu, S.; Chen, Z.; Huang, W.; Li, C.; Liu, R.; Fu, R.; Wu, D. A Robust All-Organic Protective Layer towards Ultrahigh-Rate and Large-Capacity Li Metal Anodes. *Nat. Nanotechnol.* **2022**, *17* (6), 613–621. https://doi.org/10.1038/s41565-022-01107-2.
- (39) Shi, J.; Vincent, C. A. The Effect of Molecular Weight on Cation Mobility in Polymer Electrolytes. *Solid State Ion.* **1993**, *60* (1), 11–17. https://doi.org/10.1016/0167-2738(93)90268-8.
- (40) Jakubowski, W.; Matyjaszewski, K. Activators Regenerated by Electron Transfer for Atom-Transfer Radical Polymerization of (Meth)Acrylates and Related Block Copolymers. *Angew. Chem. Int. Ed.* 2006, 45 (27), 4482–4486. https://doi.org/10.1002/anie.200600272.
- (41) Matyjaszewski, K.; Jakubowski, W.; Min, K.; Tang, W.; Huang, J.; Braunecker, W. A.; Tsarevsky, N. V. Diminishing Catalyst Concentration in Atom Transfer Radical Polymerization with Reducing Agents. *Proc. Natl. Acad. Sci.* 2006, 103 (42), 15309–15314. https://doi.org/10.1073/pnas.0602675103.

- (42) Yan, J.; Pan, X.; Wang, Z.; Zhang, J.; Matyjaszewski, K. Influence of Spacers in Tetherable Initiators on Surface-Initiated Atom Transfer Radical Polymerization (SI-ATRP).

 Macromolecules 2016, 49 (23), 9283–9286. https://doi.org/10.1021/acs.macromol.6b02273.
- (43) Yan, J.; Kristufek, T.; Schmitt, M.; Wang, Z.; Xie, G.; Dang, A.; Hui, C. M.; Pietrasik, J.; Bockstaller, M. R.; Matyjaszewski, K. Matrix-Free Particle Brush System with Bimodal Molecular Weight Distribution Prepared by SI-ATRP. *Macromolecules* 2015, 48 (22), 8208–8218. https://doi.org/10.1021/acs.macromol.5b01905.
- (44) Yan, J.; Pan, X.; Schmitt, M.; Wang, Z.; Bockstaller, M. R.; Matyjaszewski, K. Enhancing Initiation Efficiency in Metal-Free Surface-Initiated Atom Transfer Radical Polymerization (SI-ATRP). ACS Macro Lett. 2016, 5 (6), 661–665. https://doi.org/10.1021/acsmacrolett.6b00295.
- (45) Szczepaniak, G.; Jeong, J.; Kapil, K.; Dadashi-Silab, S.; Yerneni, S. S.; Ratajczyk, P.; Lathwal, S.; Schild, D. J.; Das, S. R.; Matyjaszewski, K. Open-Air Green-Light-Driven ATRP Enabled by Dual Photoredox/Copper Catalysis. *Chem. Sci.* 2022, *13* (39), 11540–11550. https://doi.org/10.1039/D2SC04210J.
- (46) Pelt, D. M.; Gürsoy, D.; Palenstijn, W. J.; Sijbers, J.; De Carlo, F.; Batenburg, K. J. Integration of TomoPy and the ASTRA Toolbox for Advanced Processing and Reconstruction of Tomographic Synchrotron Data. *J. Synchrotron Radiat.* **2016**, *23* (3), 842–849. https://doi.org/10.1107/S1600577516005658.
- (47) Wood, K. N.; Noked, M.; Dasgupta, N. P. Lithium Metal Anodes: Toward an Improved Understanding of Coupled Morphological, Electrochemical, and Mechanical Behavior. *ACS Energy Lett.* **2017**, *2* (3), 664–672. https://doi.org/10.1021/acsenergylett.6b00650.

- (48) Sturm, J.; Friedrich, S.; Genies, S.; Buzon, D.; G, R.-K.; Rheinfeld, A.; A, J. Experimental Analysis of Short-Circuit Scenarios Applied to Silicon-Graphite/Nickel-Rich Lithium-Ion Batteries. *J. Electrochem. Soc.* **2022**, *169* (2), 020569. https://doi.org/10.1149/1945-7111/ac51f3.
- (49) Zhang, X.; Sahraei, E.; Wang, K. Li-Ion Battery Separators, Mechanical Integrity and Failure Mechanisms Leading to Soft and Hard Internal Shorts. *Sci. Rep.* **2016**, *6* (1), 32578. https://doi.org/10.1038/srep32578.
- (50) Lewis, J. A.; Cortes, F. J. Q.; Liu, Y.; Miers, J. C.; Verma, A.; Vishnugopi, B. S.; Tippens, J.; Prakash, D.; Marchese, T. S.; Han, S. Y.; Lee, C.; Shetty, P. P.; Lee, H.-W.; Shevchenko, P.; De Carlo, F.; Saldana, C.; Mukherjee, P. P.; McDowell, M. T. Linking Void and Interphase Evolution to Electrochemistry in Solid-State Batteries Using Operando X-Ray Tomography. *Nat. Mater.* 2021, 20 (4), 503–510. https://doi.org/10.1038/s41563-020-00903-2.
- (51) Veeraraghavan, V. D.; Frenck, L.; Maslyn, J. A.; Loo, W. S.; Parkinson, D. Y.; Balsara, N. P. Evolution of Protrusions on Lithium Metal Anodes Stabilized by a Solid Block Copolymer Electrolyte Studied Using Time-Resolved X-Ray Tomography. ACS Appl. Mater. Interfaces 2021, 13 (23), 27006–27018. https://doi.org/10.1021/acsami.1c04582.
- (52) Harry, K. J.; Liao, X.; Parkinson, D. Y.; Minor, A. M.; Balsara, N. P. Electrochemical Deposition and Stripping Behavior of Lithium Metal across a Rigid Block Copolymer Electrolyte Membrane. *J. Electrochem. Soc.* 2015, 162 (14), A2699. https://doi.org/10.1149/2.0321514jes.

- (53) Zenyuk, I. V. Bridging X-Ray Computed Tomography and Computational Modeling for Electrochemical Energy-Conversion and –Storage. *Curr. Opin. Electrochem.* **2019**, *13*, 78–85. https://doi.org/10.1016/j.coelec.2018.10.016.
- (54) Xiao, J.; Li, Q.; Bi, Y.; Cai, M.; Dunn, B.; Glossmann, T.; Liu, J.; Osaka, T.; Sugiura, R.; Wu, B.; Yang, J.; Zhang, J.-G.; Whittingham, M. S. Understanding and Applying Coulombic Efficiency in Lithium Metal Batteries. *Nat. Energy* **2020**, *5* (8), 561–568. https://doi.org/10.1038/s41560-020-0648-z.
- (55) Li, Y.; Yang, Z.; Wu, Z.; Li, J.; Zou, J.; Jiang, C.; Yang, J.; Wang, L.; Niu, X. The Effects of Lithium Salt and Solvent on Lithium Metal Anode Performance. *Solid State Ion.* **2018**, *324*, 144–149. https://doi.org/10.1016/j.ssi.2018.06.017.
- (56) Masias, A.; Felten, N.; Garcia-Mendez, R.; Wolfenstine, J.; Sakamoto, J. Elastic, Plastic, and Creep Mechanical Properties of Lithium Metal. *J. Mater. Sci.* 2019, 54 (3), 2585–2600. https://doi.org/10.1007/s10853-018-2971-3.
- (57) Yang, Q.; Li, W.; Dong, C.; Ma, Y.; Yin, Y.; Wu, Q.; Xu, Z.; Ma, W.; Fan, C.; Sun, K. PIM-1 as an Artificial Solid Electrolyte Interphase for Stable Lithium Metal Anode in High-Performance Batteries. *J. Energy Chem.* **2020**, *42*, 83–90. https://doi.org/10.1016/j.jechem.2019.06.012.
- (58) Wang, L.; Zhao, Y.; Fan, B.; Carta, M.; Malpass-Evans, R.; McKeown, N. B.; Marken, F. Polymer of Intrinsic Microporosity (PIM) Films and Membranes in Electrochemical Energy Storage and Conversion: A Mini-Review. *Electrochem. Commun.* 2020, 118, 106798. https://doi.org/10.1016/j.elecom.2020.106798.

- (59) Xu, R.; Zhang, X.-Q.; Cheng, X.-B.; Peng, H.-J.; Zhao, C.-Z.; Yan, C.; Huang, J.-Q. Artificial Soft–Rigid Protective Layer for Dendrite-Free Lithium Metal Anode. *Adv. Funct. Mater.* **2018**, *28* (8), 1705838. https://doi.org/10.1002/adfm.201705838.
- (60) Tikekar, M. D.; Li, G.; Archer, L. A.; Koch, D. L. Electroconvection and Morphological Instabilities in Potentiostatic Electrodeposition across Liquid Electrolytes with Polymer Additives. J. Electrochem. Soc. 2018, 165 (16), A3697. https://doi.org/10.1149/2.0271816jes.
- (61) Qiu, Z.; Yuan, S.; Wang, Z.; Shi, L.; Jo, J. H.; Myung, S.-T.; Zhu, J. Construction of Silica-Oxygen-Borate Hybrid Networks on Al2O3-Coated Polyethylene Separators Realizing Multifunction for High-Performance Lithium Ion Batteries. *J. Power Sources* 2020, 472, 228445. https://doi.org/10.1016/j.jpowsour.2020.228445.
- (62) Srivastava, S.; Agarwal, P.; Archer, L. A. Tethered Nanoparticle–Polymer Composites:

 Phase Stability and Curvature. *Langmuir* **2012**, *28* (15), 6276–6281.

 https://doi.org/10.1021/la2049234.

TOC Image

